Supplementary Information (SI) for Energy & Environmental Science.

Electronic Supplementary Information (ESI)

Self-thermoregulating current collectors: built-in thermal protection for safe lithium-ion batteries

Yitong Peng, Tao Meng, Pingan Li, Rongxin Li, and Xianluo Hu*

State Key Laboratory of Materials Processing and Die & Mould Technology, School of Materials Science and Engineering, Huazhong University of Science and Technology, 430074 Wuhan, China

*Correspondence to: huxl@mail.hust.edu.cn

Experimental details

Chemicals

H62 brass foils with different thicknesses were purchased from Htiger Group, China. Sulfuric acid (98%), phosphoric acid (>85%), and cupric sulfate (>99%) were purchased from Sinopharm Chemical Reagent Co., China. Paraffin wax was provided from Ruhr Tech., China. All of the materials and reagents were used directly without further purification.

Fabrication of TCC

The preparation of the TCC involves three main steps: chemical/electrochemical etching, capillary infusion, and electroplating. A commercially available H62 brass foil (36 wt% Zn, 20 μm, Htiger Group, China) was ultrasonically cleaned with acetone and then immersed in a 1 M H_2SO_4 + 1 M H_3PO_4 solution at 90 °C until bubbling ceased. This step produced pre-treated porous copper (p-Cu). The porous copper was then electrochemically dealloyed using an electrolyte solution of 0.5 M $CuSO_4$ + 0.5 M H_2SO_4 with an applied current density of 1 mA cm^{-2} for 2 h. The porosity of the resulting p-Cu was carefully controlled at approximately 65% to ensure high filling rates and good mechanical properties. The p-Cu was immersed in molten PCM of PW (Ruhr Tech., China) and placed in a vacuum oven at 60 °C for 5 min. After infusion, the PW-filled porous copper was placed between two sheets of polyethylene filter paper with a 2 μm pore size and hot-pressed for 3 min to remove excess PW from the surface to obtain p-Cu/PW. The hot-pressing conditions were set at 0.15 kPa and 70 °C. Finally, the p-Cu/PW was electroplated using a commercially available Cu electroplating solution (ZHONGDE METAL Group Co., China) with a current density of 2 mA cm^{-2} for 45 min. The optimal electroplating time was determined based on the high electrical conductivity and low areal density of the composite film (Fig. S24). For thicker 30 μm and 50 μm brass foils, the chemical etching time was increased to 72 h and 108 h, and the current density for electrochemical etching was increased to 1.5 mA cm^{-2} and 2.5 mA cm^{-2}, respectively, with the remaining operations unchanged.

Characterization techniques

The morphology of the as-prepared TCC was observed using field-emission scanning electron microscopy (FE-SEM, Hitachi S-3500, Japan). X-ray diffraction (XRD) patterns were measured with an Empyrean diffractometer (Holland). Fourier-transform infrared spectroscopy with attenuated total reflectance (FTIR-ATR) was conducted using a Bruker ALPHA spectrometer (Germany). The pore distribution and porosity of the samples were measured using an AutoPore 9500 mercury porosimeter (Micromeritics, USA). Thermal conductivity was determined by the hotdisk method using the Hot Disk TPS 2500S (China). Tensile stress and strain of the TCC and copper foil were measured with a universal tensile tester (NSS, China). Differential scanning calorimetry (DSC200F3, Netzsch, Germany) was performed to characterize the heat-storage capacity and specific heat of the samples, ranging from 30 °C to 60 °C at a heating rate of 5 °C min^{-1}. Thermographic images were captured with an infrared imager (D384A, GUIDE INFRARED).

Electrode preparation and cell assembly

Gr (Asahi Kasei, Japan) was coated on both the commercial 11-μm Cu foil and the TCC using a standard slurry coating process. The slurry consisted of Gr, Super P conductive carbon black, and polyvinylidene fluoride (PVDF) in a weight ratio of 80 : 10 : 10 mixed with N-methyl-2-pyrrolidone as the solvent. The as-prepared Gr electrodes were pressed to 0.8 g cm^{-3}. 10-mm diameter electrodes were punched from the prepared graphite electrodes and assembled into 2032-type coin cells. The electrolyte used was a commercial carbonate-based liquid electrolyte (LB-015) containing 1 M $LiPF_6$ in ethylene carbonate (EC) and diethyl carbonate (DEC) (1:1 volume ratio), with an additional 5 wt% fluoroethylene carbonate (FEC), from DoDoChem. The amount of electrolyte used was 40 μL for coin cells and 3 g Ah^{-1} for $LiFePO_4$||Gr pouch-type cells. To highlight the deteriorating effect of high temperature on the vulnerable Gr-electrolyte interface, a reduced amount of electrolyte (2.0 g Ah^{-1}) was injected into the $LiNi_{0.8}Mn_{0.1}Co_{0.1}O_2$ (NMC811)||Gr pouch cells. Polyethylene (Celgard 2500) served as the separator. The counter electrode was a 750-μm thick lithium metal foil with a 15-

mm diameter. For the full cell assembly, the positive electrode consisted of a $LiFePO_4$ electrode from Canrd New Energy Technology Co., Ltd., with a composition of $LiFePO_4$: Super P conductive carbon black: PVDF = 93.5 :3.5 : 3 wt%. The double-sided coated NMC811 positive electrode was obtained from Wuhan Chuangneng New Energy Technology Co., Ltd., with a composition of NMC811:Super P conductive carbon black:CNT:PVDF = 96.8:1.5:0.4:1.3 wt%. For the $LiFePO_4$||Gr cell, the areal loadings of the $LiFePO_4$ and Gr electrodes were 13.2 and 5.8 mg cm^{-2}, respectively. For the NMC811||Gr cell, the areal loadings of the NMC811 and Gr electrodes were 12.5 and 8.2 mg cm^{-2}, respectively.

Electrochemical measurements

For all cell tests, five activation cycles at 0.1C were conducted to ensure optimal lithium-ion insertion into the graphite and to form a SEI layer on the Gr surface. In Gr||Li half-cells, the voltage range was set between 0.005 and 2.000 V (versus Li/Li^+), using an electrochemical analyzer from Landt, China. For $LiFePO_4$||Gr full cells, the voltage range was cycled between 2.00 and 3.65 V. When the charge rate exceeded 1C, the charging mode was switched from constant current (CC) to constant current and constant voltage (CC & CV) to ensure the battery was fully charged. The cut-off current during constant voltage charging was set at 0.02C. For NMC811||Gr full cells, the voltage range was cycled between 2.50 and 4.20 V. All tests were conducted at an ambient temperature of 28 °C. For the pouch cells used in the heat production experiments, after completing the activation process, the cells were fully charged at a rate of 0.2C. Electrochemical impedance spectroscopy (EIS) was used to measure impedance changes over a frequency range of 0.1 Hz to 100 kHz. CV curves for the Gr||Li cell were tested within a voltage range of 0.005 to 2.000 V at a scan rate of 0.2 0.2 mV s^{-1}. All these measurements were conducted using a CHI 660D electrochemical workstation from Chenhua Instruments Co., China. The DCR test protocol is as follows: The fully charged cell was first discharged at 4C for 10 s, then discharged at 1C to 10% of the total capacity, followed by a 30-min rest. This process was repeated to obtain DCR values at different states of charge. The DCR value is defined as:

$$DCR = \frac{U_1 - U_2}{I_{4C}} \quad (1)$$

where U_1 represents the open-circuit voltage of the cell before the 4C discharge, and U_2 represents the instantaneous voltage at the end of the 4C discharge.

Thermoregulation analysis

The nail penetration test to simulate an internal short circuit was conducted on fully-charged, dual-layer $LiFePO_4$||Gr pouch-type cells with a capacity of 110 mAh. The pouch cells were assembled using $LiFePO_4$ electrodes (43 mm × 56 mm), polypropylene (PP) separators (47 mm × 60 mm), and graphite electrodes (45 mm × 58 mm). Prior to the test, the cells were galvanostatically charged to a 100% state of charge. A 5-mm diameter nail was then driven at a speed of 80 mm s^{-1} through the center of the fully charged cells. During the test, the cell temperatures were monitored using an infrared camera and thermocouples, while the cell voltage was detected by an electrochemical workstation. A pseudo-adiabatic environment for the battery was created using the adiabatic mode of an accelerating rate calorimeter (BAC-90A, Young Instrument, China). In addition, to enhance heat generation within the battery, a 0.5C discharge was performed using fully charged five-layer $LiFePO_4$||Gr pouch-type cells with a capacity of 225 mAh. The initial temperature of the ARC chamber was set to 30°C. Once the temperature reached the set value, it was maintained for 30 minutes, followed by the cell starting to discharge. The thermocouple was placed at the center of the battery. When ARC detected that the temperature rise rate of the battery exceeded 0.02 °C min^{-1}, the pseudo-adiabatic mode was activated. This mode was stopped when the thermocouple measured that the battery temperature remained stable for 3 min, indicating no further temperature increase. During the 4C-discharge cycling, the cell was first fully charged at 1C constant current and constant voltage with a cut-off current of 0.05C, followed by a rapid discharge at 4C to quickly release heat. After each discharge, the battery was allowed to stand for 15 min to return to room temperature before recharging.

Finite element analysis

All the models and numerical calculations were performed using the finite element software of COMSOL Multiphysics 5.4. For this analysis, we selected 88 mm × 70 mm soft-type cells and 18650 cylindrical batteries as the analytical models. This electrochemical-thermal coupling model is based on a Pseudo-two-dimensions (P2D) electrochemical model and a three-dimensional thermal model,[1,2] comprising a set of mutually coupled nonlinear partial differential equations that describe ion diffusion processes in both solid and liquid phases, as well as charge and heat conservation. The electrochemical and thermal fields are coupled through rapid bidirectional feedback of heat generation power Q and temperature T variables (Fig. S25). The electrochemical and thermodynamic formulas used in the model, along with the corresponding boundary conditions, are detailed in Table S3. The parameter values employed in the model are provided in Table S4.

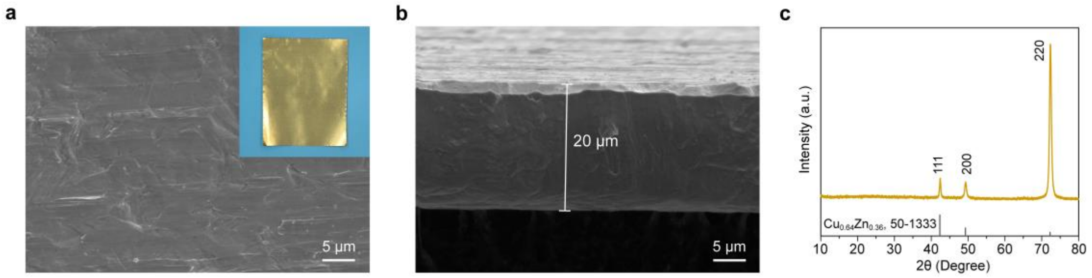

Fig. S1 Morphology and phase analysis of brass. Surface (**a**) and cross-sectional (**b**) SEM images of brass foil. The inner illustration shows the display of brass foil. (**c**) XRD analysis of brass foil.

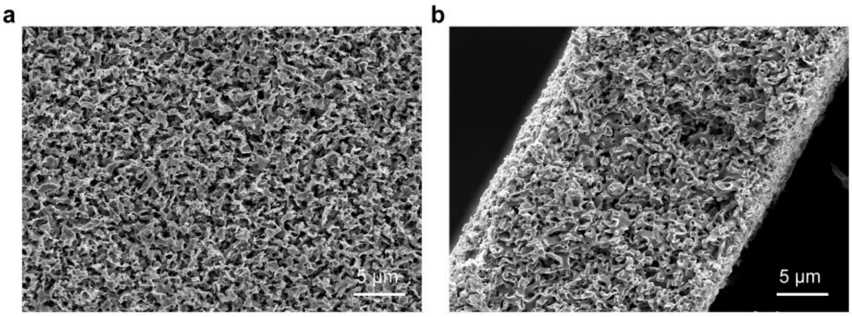

Fig. S2 Morphology of the p-Cu. Surface (**a**) and cross-sectional **(b)** SEM images of p-Cu film before filling.

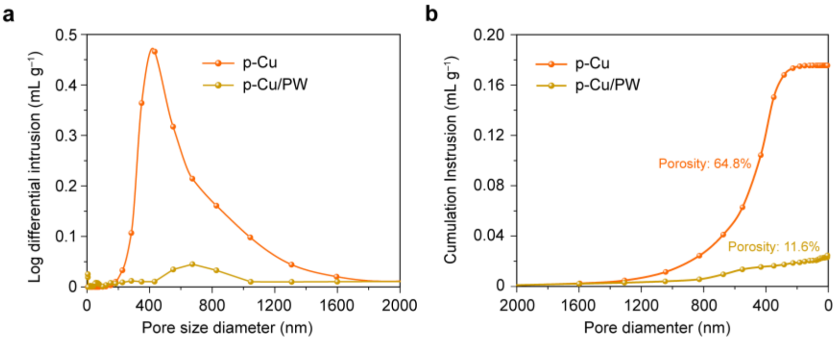

Fig. S3 Pore characteristics before and after PW filling. Pore distribution (**a**) and porosity (**b**) of p-Cu and p-Cu/PW by mercury intrusion method.

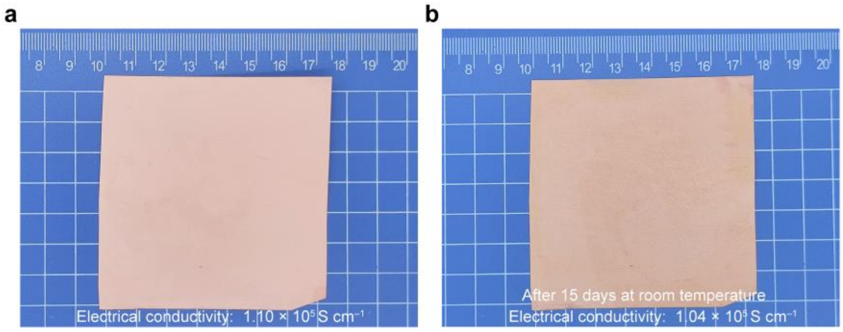

Fig. S4 Antioxidant test of TCC. (**a**) Digital camera pictures of fresh TCC; (**b**) Stored TCC after 15 days at room temperature.

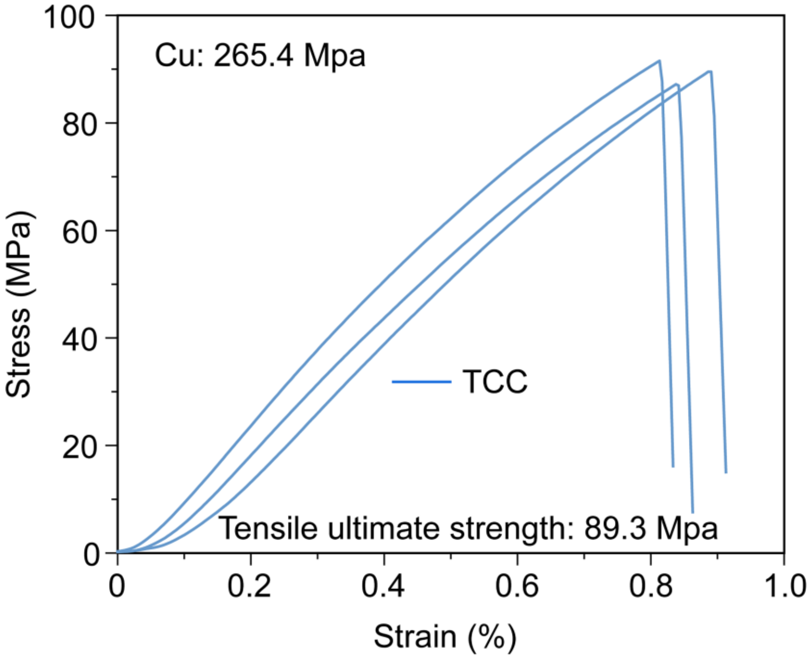

Fig. S5 Tensile curves of TCC.

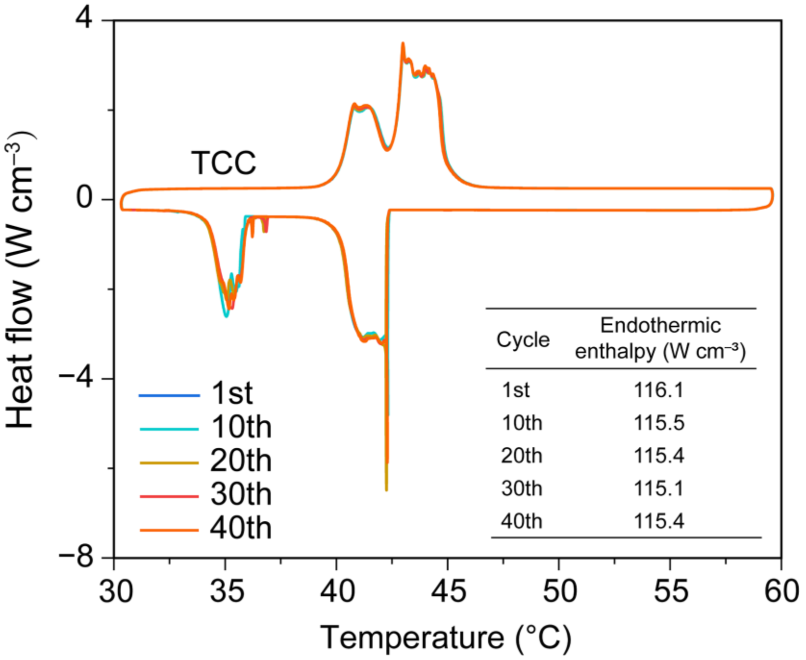

Cycle	Endothermic enthalpy (W cm⁻³)
1st	116.1
10th	115.5
20th	115.4
30th	115.1
40th	115.4

Fig. S6 Cycling DSC results of TCC.

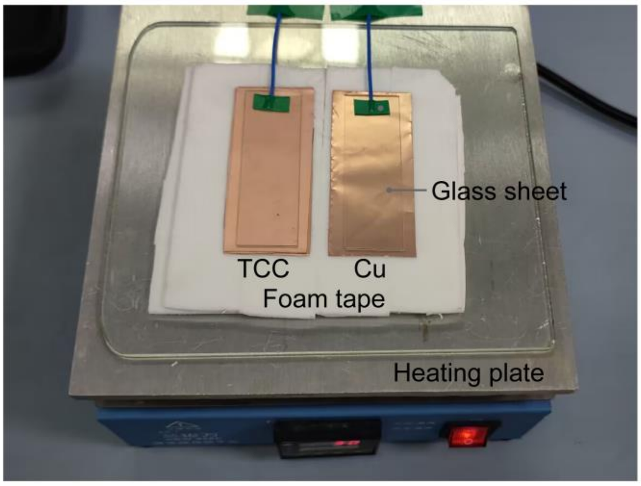

Fig. S7 Digital camera pictures for the thermal storage test.

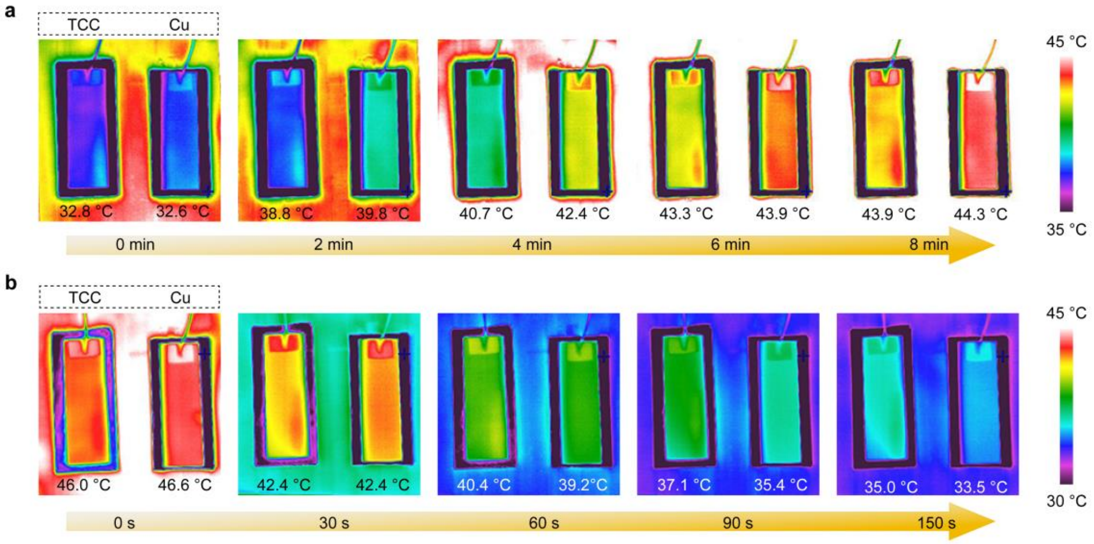

Fig. S8 Thermal imaging of glass slides during heating (**a**) and cooling (**b**) processes for both TCC and Cu foil.

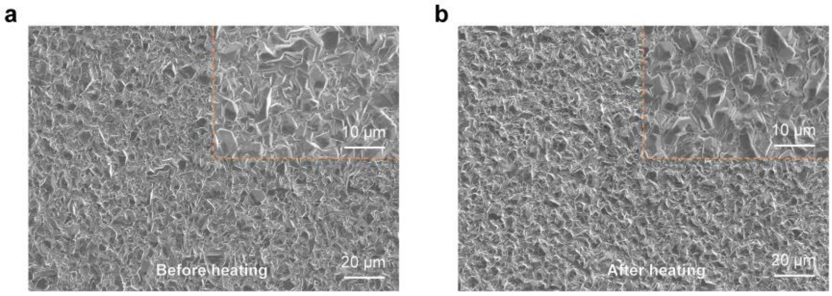

Fig. S9 SEM images of TCC before (**a**) and after (**b**) The surface of TCC remained smooth and clean without paraffin leakage.

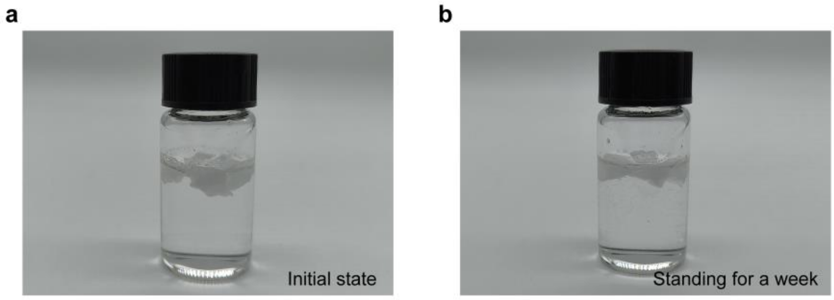

Fig. S10 Photographs of PW before (**a**) and after (**b**) soaking in the electrolyte at ambient temperature for a week. The insolubility of PW ensures the durability of TCC.

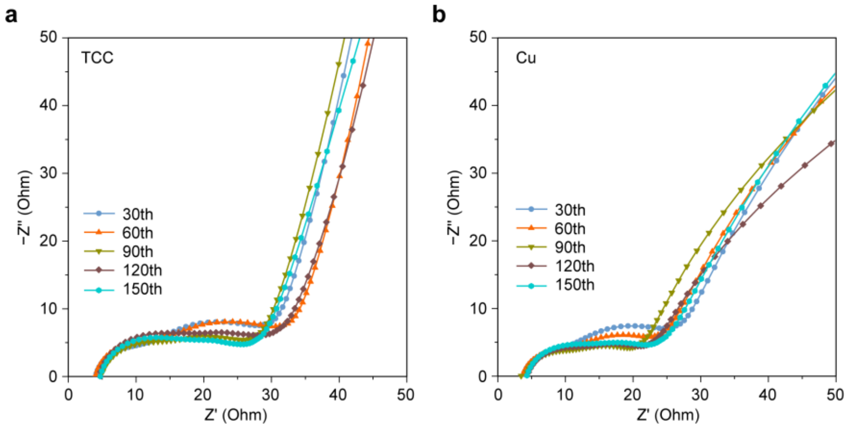

Fig. S11 EIS results of Gr/Li half-cells assembled with TCC (**a**) and Cu (**b**) during the cyclic process. The results of EIS show that the impedance of TCC-assembled Gr||Li cell display minimal changes during cycling and are basically consistent with that of the Cu-assembled cell, which confirms the good cycle performance of the TCC-assembled Gr/Li cell.

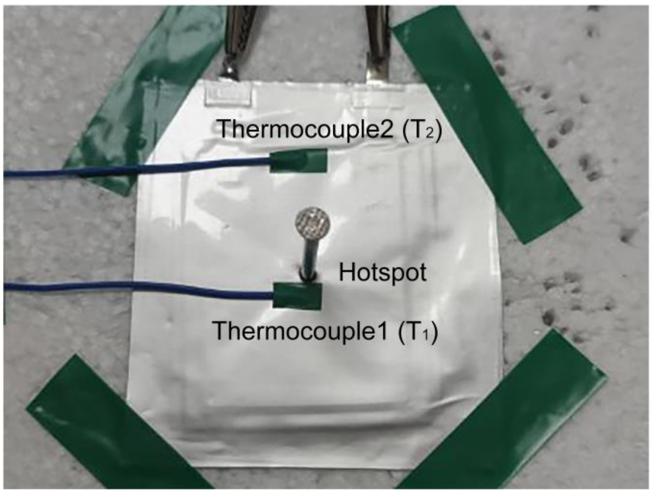

Fig. S12 Physical display of the needle penetration test. The thermoregulating capability of TCC is expected to effectively delay battery temperature rise, especially in dealing with local hot spots.

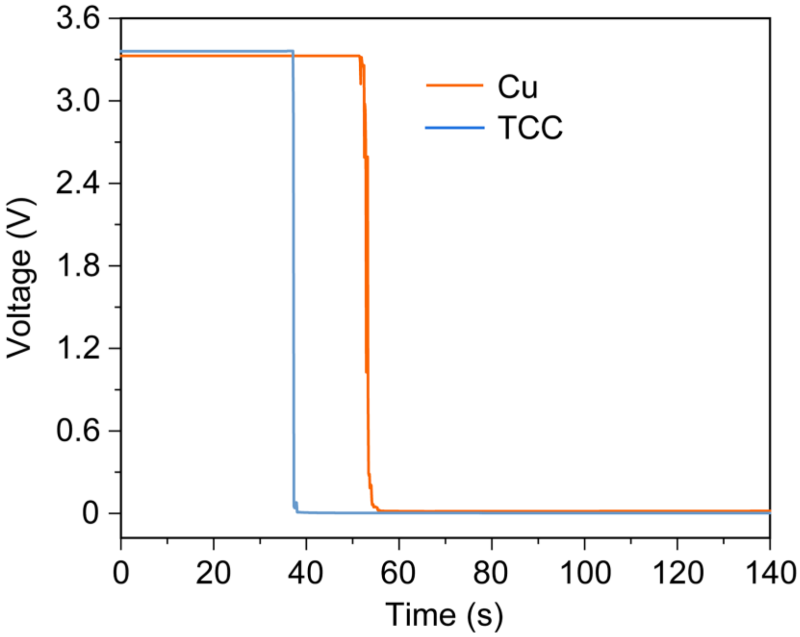

Fig. S13 Changes in battery voltage after needle penetration.

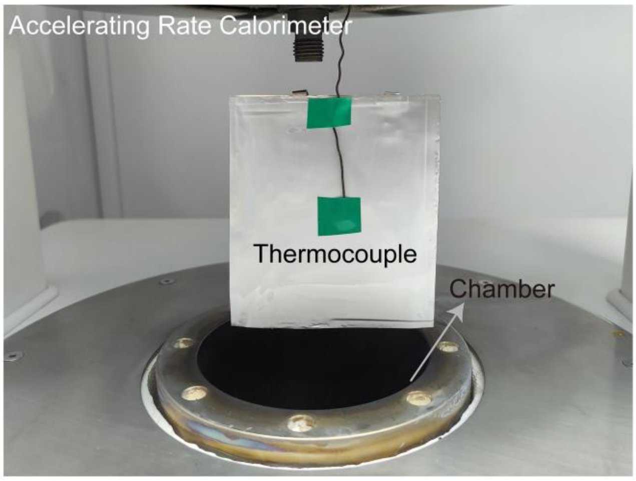

Fig. S14 Digital camera picture of the ARC adiabatic mode. Considering negligible heat exchange between the cells and surroundings, the disparity in temperature can be attributed entirely to the thermoregulating effect of TCC.

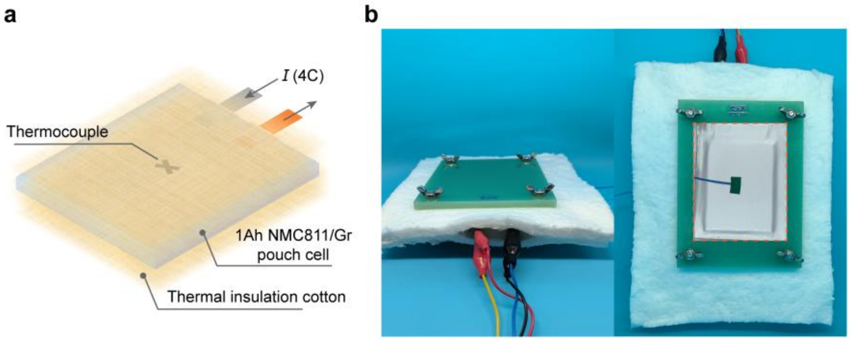

Fig. S15 Schematic illustration (**a**) and physical display (**b**) of 4C-discharge cycle test of 1-Ah NMC811/Gr pouch cell. The pouch cell is placed between two layers of 10-mm commercial aluminum silicate thermal insulation cotton to provide a poorly heat-dissipating environment. The thermocouple is placed at the center of the cell to monitor the temperature during discharge.

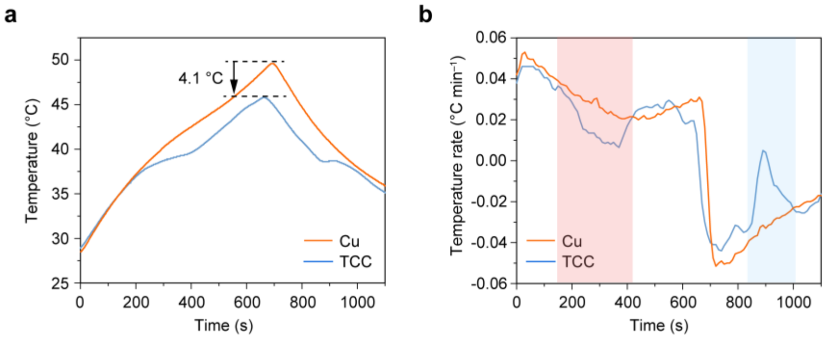

Fig. S16 Temperature-time curves (**a**) and the temperature rate-time curves (**b**) during the first 4C-discharge process of the batteries assembled with TCC and Cu. The red and blue shadings represent that TCC absorb and release heat, respectively.

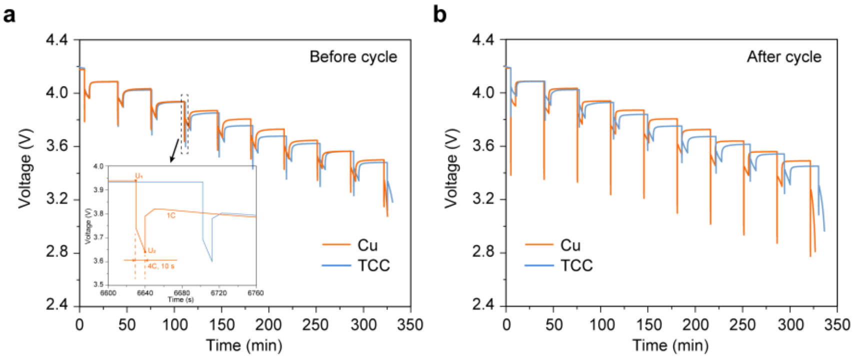

Fig. S17 Voltage-time curve of batteries in DCR test.

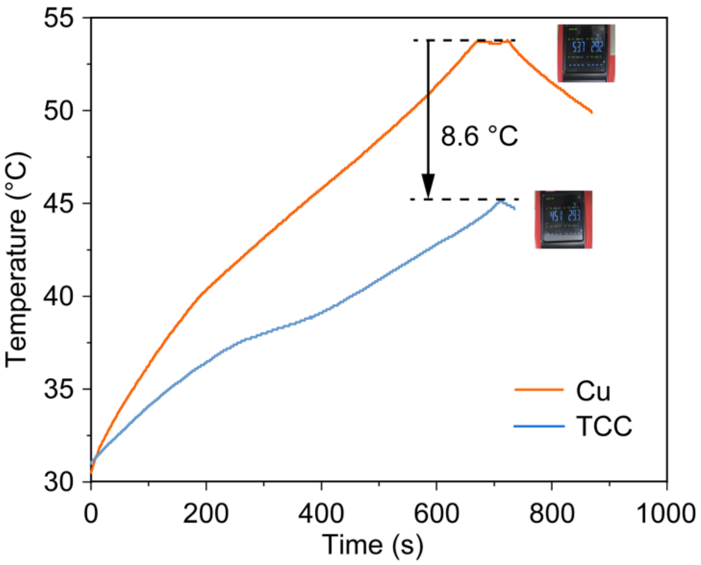

Fig. S18 Temperature-time curves during the 4C-discharge process of the cells assembled with TCC and Cu at the 85th cycle.

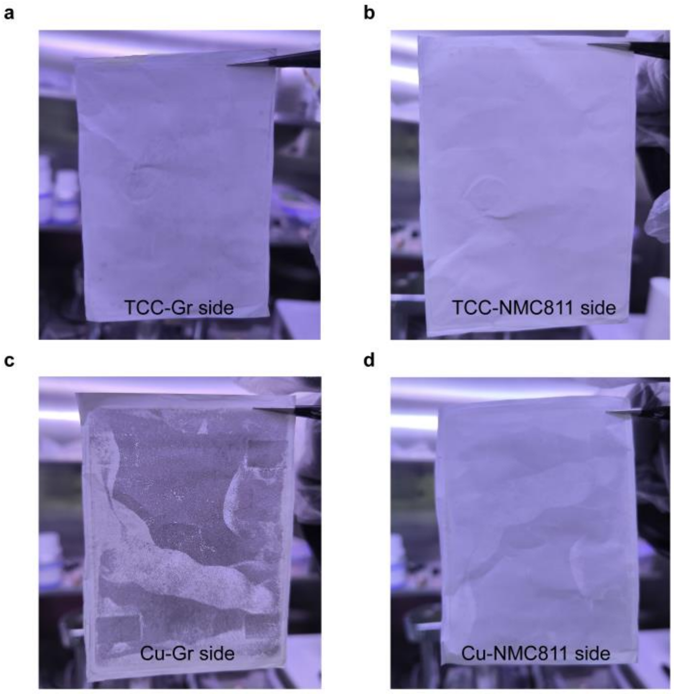

Fig. S19 Optical images for the separator after cycle. Gr side (a, c) and NMC811 side (b, d) of the separator of the TCC-assembled and Cu-assembled cells.

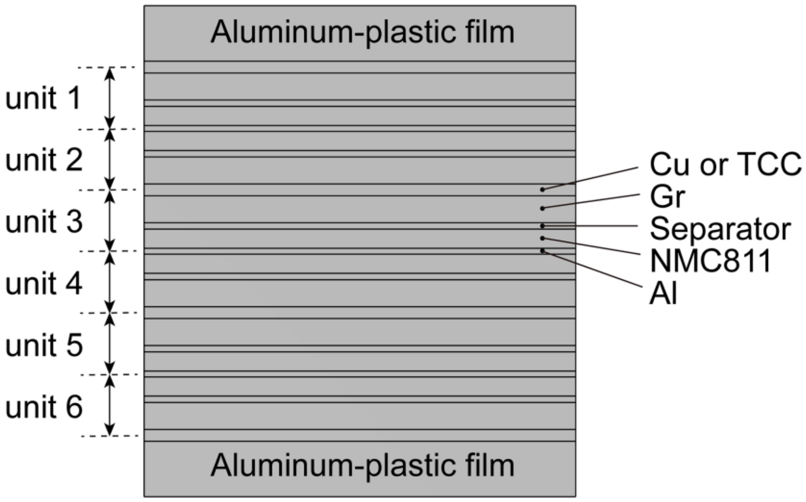

Fig. S20 Cross-section schematic illustration of the pouch cell model. The model contains six repeating units, and each includes a positive current collector (Al), a negative current collector (Cu or TCC), a NMC811 electrode, an Gr electrode, and a separator.

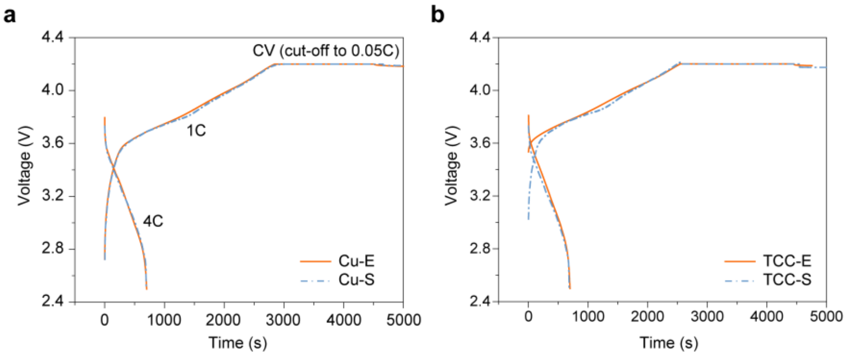

Fig. S21 Experimental and simulated charge-discharge curves of 1-Ah NMC811||Gr pouch cells assembled with Cu **(a)** and TCC **(b)**.

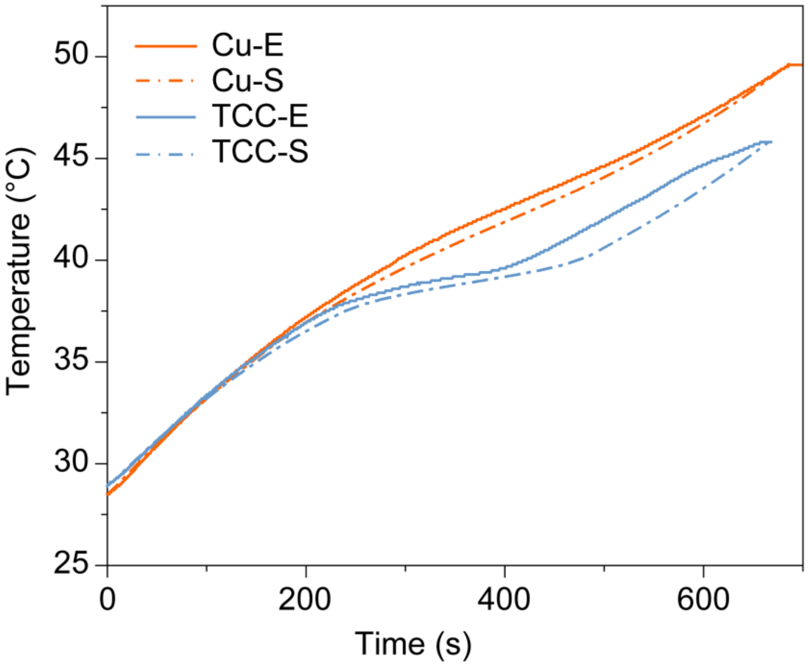

Fig. S22 Experimental and simulated temperature-time curves of 1-Ah NMC811||Gr pouch cells assembled with Cu and TCC during the first 4C-discharge.

Fig. S23 Simulation illustration of heat generation during discharging process. The heating area is the entire jelly roll, including the positive electrode, negative electrode, separator, and current collector areas. The non-heating area is the stainless-steel casing and nylon core.

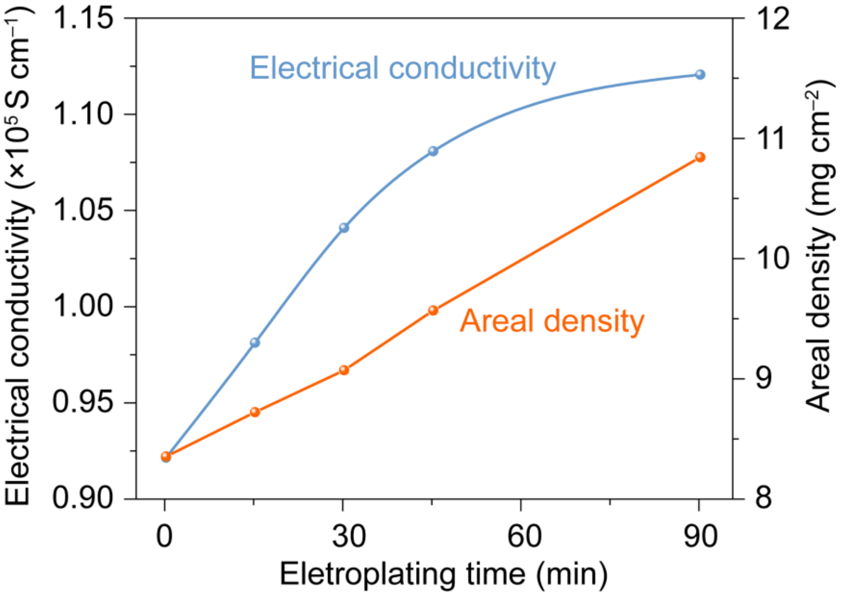

Fig. S24 Correlation curves illustrating the relationship between electroplating time and the electrical conductivity and areal density of composite films.

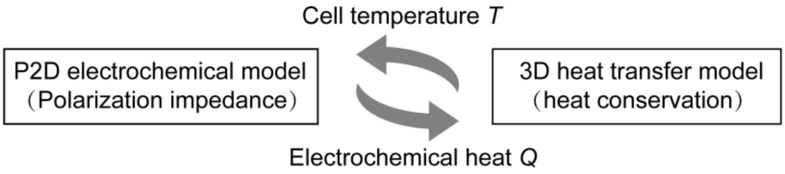

Fig. S25 Schematic diagram of the electrochemical-thermal coupling model.

To demonstrate the potential applicability of TCC in existing high-energy LIBs, we calculated the thermoregulating capability of TCC on batteries based on its latent heat value and the weight, density, and specific heat capacity of each battery component (presented in Table S1). To reflect the scalability of TCC design, we prepared different TCCs using brass foils with varying thicknesses as raw materials. The preparation methods of all TCCs were consistent, and the porosity of porous Cu skeleton was maintained at 65%. These TCCs were named according to the thickness of the brass foil used, such as TCC-20 representing a 20 μm brass foil as raw material. Due to the double-side coating of the electrodes, the repeating unit of the cell L_{unit} can be regarded as:

$$L_{unit} = L_{\text{pos\_cc}}/2 + L_{\text{pos}} + L_{\text{sep}} + L_{\text{neg}} + L_{\text{neg\_cc}}/2 \tag{2}$$

Where, L_{pos_cc}, L_{pos}, L_{sep}, L_{neg}, and $L_{\text{neg\_cc}}$ represent the thickness of positive current collector, single-side positive electrode layer, separator, single-sided negative electrode layer, and negative current collector, respectively. Therefore, the thermoregulating capability of TCC T_{c} can be expressed as follows:

$$T_{\text{c}} = \frac{m_{\text{TCC}} L_{\text{TCC}}}{\sum_i m_i (C_p)_i} \tag{3}$$

Where, m_{TCC} and L_{TCC} represent the area mass and specific latent heat value of TCC, respectively. The variable i represents all components of the cell, including aluminum foil, single-side NCM811 electrode layer, separator, single-sided Gr electrode layer, and TCC.

Table S1. Calculated thermoregulating capacity of TCC and the corresponding cell parameters

Cell components	**Cell parameter**	
NCM811 cathode	Areal capacity (mAh cm^{-2} each side)	2.26
	Active materials content	94%
	Coating weight (mg cm^{-2} each side)	12
	Discharge capacity (mAh g^{-1})	220
	Coating thickness (μm)	81
	Specific heat capacity (J kg^{-1} K^{-1})	1270
Gr anode	Areal capacity (mAh cm^{-2} each side)	2.35

		Active materials content	96
		Coating weight (mg cm^{-2} each side)	6.9
		Discharge capacity (mAh g^{-1})	355
		Coating thickness (μm)	62
		Specific heat capacity (J kg^{-1} K^{-1})	1437
Separator		Separator weight (mg cm^{-2})	1.0
		Thickness (μm)	25
		Specific heat capacity (J kg^{-1} K^{-1})	1978
Electrolyte		Electrolyte/capacity (g Ah^{-1})	1.5
		Electrolyte weight (mg cm^{-2})	3.2
		Specific heat capacity (J kg^{-1} K^{-1})	133.9
Collectors (half)	Copper foil	Areal weight (mg cm^{-2})	4.4
		Thickness (μm)	5.5
		Specific heat capacity (J kg^{-1} K^{-1})	385
	TCC-20	Areal weight (mg cm^{-2})	4.8
		Thickness (μm)	12
		Specific heat capacity (J kg^{-1} K^{-1})	368.1
		Latent heat (J cm^{-3}/J g^{-1})	116.1/29.2
	TCC-30	Areal weight (mg cm^{-2})	6.9
		Thickness (μm)	17
		Specific heat capacity (J kg^{-1} K^{-1})	367.7
		Latent heat (J cm^{-3}/J g^{-1})	124.6/30.7
	TCC-50	Areal weight (mg cm^{-2})	11.0
		Thickness (μm)	27
		Specific heat capacity (J kg^{-1} K^{-1})	367.1
		Latent heat (J cm^{-3}/J g^{-1})	129.8/31.9
	Aluminum foil	Areal weight (mg cm^{-2})	2.7
		Thickness (μm)	10
		Specific heat capacity (J kg^{-1} K^{-1})	903
Cell		Nominal voltage (V)	3.9
		N/P ratio	1.04~1.06
Gravimetric energy density (Wh Kg^{-1})		Copper foil	292.1
		TCC-20	288.3
		TCC -30	270.0
		TCC-50	240.0
Volumetric energy density (Wh L^{-1})		Copper foil	480.3
		TCC-20	463.9
		TCC-30	452.0
		TCC-50	430.0
Deterioration in gravimetric energy density (%)		TCC-20	1.3
		TCC-30	7.6
		TCC-50	17.8
		TCC-20	3.4

Deterioration in volumetric energy density (%)	TCC-30	5.9
	TCC-50	10.5
Thermoregulating capability *T*c (°C)	TCC-20	4.5
	TCC-30	6.5
	TCC-50	10.3
a: Gravimetric energy density = the theoretical capacity * nominal voltage / total mass of all components; b: Volumetric energy density = the theoretical capacity * nominal voltage / total volume of all components.		

Table S2. Specifications of NCM811/graphite battery used for simulation

Battery basic characteristics	Value
Theoretical capacity	2.1 Ah
Type	18650
Maximum cut-off voltage	4.2 V
Minimum cut-off voltage	2.5 V
Discharge rate	3C
Cathode material	$LiNi_{0.8}Co_{0.1}Mn_{0.1}O_2$
Anode material	Graphite
Separator	Polyethylene
Electrolyte	$LiPF_6$/EC: DEC (1 : 1, by volume) 1000 mol m^{-3}
Positive current collector	20-µm Al foil
Negative current collector	11-µm Cu foil, 23-µm TCC (TCC-20)

Table S3. Summary of the governing equation and boundary conditions in the model

Physics	Expressions	Boundary conditions
Ohm's law	$-\sigma_s^{\mathrm{eff}}\frac{\partial\phi_s}{\partial x}=i_s$	$-\sigma_s^{\mathrm{eff}}\frac{\partial\phi_s}{\partial x}\Big\vert_{x=L_p+L_n+L_s+L_{p\_cc}+L_{n\_cc}}=i_{\mathrm{app}}$
Charge, solid phase	$-\frac{\partial i_s}{\partial x}=\sigma_s^{\mathrm{eff}}\frac{\partial^2\phi_s}{\partial x^2}=aFj$	$-\sigma_s^{\mathrm{eff}}\frac{\partial\phi_s}{\partial x}\Big\vert_{x=L_{n\_cc}}$ $=-\sigma_s^{\mathrm{eff}}\frac{\partial\phi_s}{\partial x}\Big\vert_{x=L_n+L_{n\_cc}+L_s+L_p}=0$
Charge, electrolyte phase	$\frac{\partial}{\partial x}\left(\sigma_e^{\mathrm{eff}}\frac{\partial\phi_e}{\partial x}\right)$ $=-aFj+\frac{2RT(1-t_+^0)}{F}\frac{\partial}{\partial x}\left(\sigma_e^{\mathrm{eff}}\frac{\partial lnc_e}{\partial x}\right)$	$-\sigma_e^{\mathrm{eff}}\frac{\partial\phi_e}{\partial x}\Big\vert_{x=L_n+L_{n\_cc}}$ $=-\sigma_e^{\mathrm{eff}}\frac{\partial\phi_e}{\partial x}\Big\vert_{x=L_n+L_{n\_cc}+L_s}=0$
Species, solid phase	$\frac{\partial c_s}{\partial t}=\frac{1}{r^2}\frac{\partial}{\partial r}\left(D_s r^2\frac{\partial c_s}{\partial r}\right)$	$-D_s\frac{\partial c_s}{\partial r}\Big\vert_{r=0}=0,-D_s\frac{\partial c_s}{\partial r}\Big\vert_{r=R_s}=j$
Species, electrolyte phase	$\varepsilon_e\frac{\partial c_e}{\partial t}=\frac{\partial}{\partial x}\left(D_e^{\mathrm{eff}}\frac{\partial c_e}{\partial x}\right)+(1-t_+^0)aj$	$-D_e^{\mathrm{eff}}\frac{\partial c_e}{\partial x}\Big\vert_{x=0}=-D_e^{\mathrm{eff}}\frac{\partial c_e}{\partial x}\Big\vert_{x=L_p+L_s+L_n}=0$
Butler-Volmer equation	$j=i_0\cdot[exp(\frac{\alpha_a F}{RT}\eta_s)-exp(-\frac{\alpha_c F}{RT}\eta_s)]$ $i_0=Fk_0c_e^{\alpha_a}\left(c_{s,max}-c_{s,surf}\right)^{\alpha_a}c_{s,surf}^{\alpha_a}$	
Overpotential for the intercalation reaction	$\eta_s=\phi_s-\phi_e-U$	
Energy balance	$\rho C_p\frac{\partial T}{\partial t}=\nabla(\lambda\nabla T)+Q$	$-k\frac{\partial T}{\partial n}\Big\vert_{\mathrm{surf}}=h\cdot(T-T_{amb})$
Heat generation	$Q=Q_{\mathrm{act}}+Q_{\mathrm{rea}}+Q_{\mathrm{ohm}}+Q_0$	
Active polarization heat generation	$Q_{\mathrm{act}}=Faj(\phi_s-\phi_e-U)$	
Reaction heat generation	$Q_{\mathrm{rea}}=FajT\frac{\partial U}{\partial T}$	

Ohmic heat generation	$Q_{\mathrm{ohm}} = \sigma_{\mathrm{eff}} \left(\frac{\partial \phi_s}{\partial x} \right)^2 + \kappa_{\mathrm{eff}} \left(\frac{\partial \phi_l}{\partial x} \right)^2 + \frac{2\kappa_{\mathrm{eff}} RT}{F} (1 - t_+^0) \frac{\partial\, ln\, c}{\partial x} \frac{\partial \phi_l}{\partial x}$

Variable Symbol	Description	Unit
ϕ_{s}	Electrical potential in the solid phase	V
ϕ_{e}	Electrical potential in the electrolyte phase	V
C_{s}	Insertion particle concentration in the solid phase	mol m^{-3}
$C_{\mathrm{s,surf}}$	Concentration of the particle surface	mol m^{-3}
C_{e}	Salt concentration in the electrolyte phase	mol L^{-3}
j	Molar flux	mol m^{-2} s^{-1}
i_{s}	Electrode current density	A m^{-2}
k	Thermal conductivity	W m^{-1} K^{-1}
ρ	Density	kg m^{-3}
C_p	Specific thermal capacity	J kg^{-1} K^{-1}
h	Convection coefficient	W m^{-2} K^{-1}
T_{amb}	Ambient temperature	K

Table S4. Summary of the parameters in the model

Symbol	Parameter	Unit	Value
F	Faraday constant	C mol^{-1}	96487
R	Ideal gas constant	J mol^{-1} K^{-1}	8.314
r_batt	Diameter of battery	mm	9
r_mandrel	Diameter of nylon mandrel	mm	2
L_wall	Thickness of stainless-steel wall	mm	0.5
H_batt	Height of battery	mm	60
h	Convection coefficient	W m^{-2} K^{-1}	60[3]
T_{amb}	Ambient temperature	K	301.15

Symbol	Parameter	Unit	Anode	Cathode	Sep	Al	Cu	TCC
L	Length	μm	64	64	30	10	10	24
R_s	Particle radius	μm	5[b]	3.77[b]				
ε_s	Volume fraction of solid phase	1	0.62[b]	0.48[b]				
ε_e	Volume fraction of electrolyte phase	1	0.31[b]	0.29[b]	0.45[b]			
σ_s	Electrical conductivity in solid phase	S m^{-1}	100[a]	3.8[a]		3.8E+7[b]	6.0E+7[b]	1.1E+7[b]
$c_{e,0}$	Initial value of Li$^+$ concentration in electrolyte phase	mol m^{-3}	1000					
$c_{s,max}$	Maximum solid phase Li$^+$ concentration	mol m^{-3}	31507[a]	50060[a]				
$c_{s,0}$	Initial value of Li$^+$ concentration in solid phase	mol m^{-3}	27904[a]	11113[a]				
x	Stoichiometry coefficient, x at 1, 0 SOC	1	0.98, 0[a]	0.942, 0.222[a]				
i_0	Exchange current density	A m^{-2}	0.96[a]	1.52[a]				
α_a, α_c	Transfer coefficients of lithium intercalation reaction	1	0.5, 0.5[4]	0.5, 0.5[4]				
k	Thermal conductivity	W m^{-1} K^{-1}	1.04[a]	1.58[a]	0.344[5]	170[a]	398[a]	167.8[b]
ρ	Density	kg m^{-3}	1347.3[a]	2328.5[a]	1009[a]	2700[a]	8933[a]	3979[b]
C_p	Specific thermal capacity	J kg^{-1} K^{-1}	1437.4[a]	1269.2[a]	1978[5]	875[a]	385[a]	365[b]

Parameter source: a. COMSOL built-in; b. measurement; [number]. reference.

References

1. L. Xu, X. Lin, Y. Xie and X. Hu, *Energy Storage Mater.*, 2022, **45**, 952-968.
2. Q.-K. Wang, J.-N. Shen, Z.-F. Ma and Y.-J. He, *Chem Eng J.*, 2021, **424**, 130308.
3. Y. Zhang, W. Zhang, W. Kong, G. Wang and X. Tang, *J Energy Storage.*, 2024, **85**, 111028.
4. W. Mu, X. Liu, Z. Wen and L. Liu, *J Energy Storage.*, 2019, **26**, 100921.
5. R. Zhao, J. Liu and J. Gu, *Appl. Energy*, 2015, **139**, 220-229.